Document downloaded from:

http://hdl.handle.net/10251/176329

This paper must be cited as:

Alcañiz, D.; Caccavale, P.; De Bonis, MV.; De Los Reyes, R.; Ortolá Ortolá, MD.; Ruocco, G. (2021). Optimal design of an innovative microwave-based fluid heater. International Journal of Thermal Sciences. 164:1-7. https://doi.org/10.1016/j.ijthermalsci.2021.106848

The final publication is available at

https://doi.org/10.1016/j.ijthermalsci.2021.106848

Copyright Elsevier

Additional Information

Optimal design of an innovative microwave-based fluid heater

Diego Alcañiz[a], Paolo Caccavale[b], Maria Valeria De Bonis[b], Ruth de los Reyes[a], Maria Dolores Ortolá[a], Gianpaolo Ruocco[b,*]

[a]Instituto Universitario de Ingenieria de Alimentos para el Desarrollo, Universitat Politècnica de València, Camino de Vera s/n, 46022 Valencia, Spain
[b]Scuola d'Ingegneria, Università degli Studi della Basilicata Campus Macchia Romana, 85100 Potenza, Italy

Abstract

New heating technologies are constantly being developed worldwide, specially the electrical ones that take advantage of renewable energy. In this paper, the Basic Cell of Energy Transference (BCET) is proposed as an innovative fluid heater, carrying a microwave-fed heat transfer plate for thermal contact. A fully-dimensional thermo-fluid analysis was implemented and validated to determine the key design parameters and operation features for heat transfer to temperature-sensitive working fluids.

Circulation patterns were observed, when using certain fluids, in turn causing strong temperature non-uniformities. As fluid treatment in the heater relies on the thermal contact at its active plate, the model was used to ascertain the undesired excess/lack temperature range for quality/safety treatments, with reference to a final effective process temperature. Therefore, a geometry optimization by means of internal baffles was carried out which ensured variation to fluid pattern and more uniform active plate temperature. In a base case, the new design allowed to limit the uncontrolled temperature excess by almost 30%, while favouring the pressure drop reduction across the flow device by more than 10%.

Keywords: Fluid Heater, Computational Fluid Dynamics, Heat transfer and fluid dynamics optimization

1. Introduction

Nowadays, new heating technologies are being developed all around the world, specially, technologies that can be feed with electricity. Over the past two decades, rapid growth in the development of adaptation responses to climate change has occurred around the world [1]. Therefore, the interest in the electrical-feed

*Corresponding author
Email address: gianpaolo.ruocco@unibas.it (Gianpaolo Ruocco)

heating in common processes (such as in the food industry) has risen considerably as it can take advantage of renewable sources of energy, and as it has far less associated CO_2 emissions than the fossil fuels technologies. Process heating is an area of interest for emission reduction as the 70% of the total energy cost of some sectors of the food industry comes from heating processes [2].

There are many novel technologies that can be used for heating applications and, specifically, to heat liquids, like ohmic heating [3], irradiation [4] or microwave (MW)[5]. One such example is the Basic Cell of Energy Transference (BCET) [6], which consists, in its simplest configuration, in two flow boxes interspersed by an active heat transfer plate. The working fluid flows sequentially through the two box, making thermal contact with the active ceramic plate, which is heated by conducted MW. Due to its specifically-designed composition and dimensions, optimized to absorb MW, the active part of the BCET provides precise, efficient and flexible operation to heat fluids in a similar way than a Plate Heat Exchanger (HEX) the most widespread device for heating fluids industrially [7]. Thanks to its compact design and working simplicity (no auxiliary fluid is necessary), it finds its application for precise liquid thermization and in rural areas installations, that can benefit of solar- or wind-driven energy and cannot depend upon a regular water supply. Its feeding technology allows for precise hold-up times, e.g. for pasteurization processes [8, 9] and finely-tuned power modulation from the active plate, e.g. with oscillating/periodic heat flux as in nanofluids thermization [10], which requires more immediate response to temperature changes.

HEX and heater design optimization is a very active area of research an development. Recently, Yang et al. [11], Picon-Nuñez et al. [12], Caputo et al. [13] confirmed that the pressure drop is correlated with the heat transfer coefficient, which is the key concept at stake here. While higher heat transfer contact and removal from the heater's active plate (or heater efficiency) is ensured by turbulent flow conditions, laminar flows are preferred instead to decrease the cost associated with pumping power [14]. On the other hand, the increment of heater efficiency, for a given active surface area, may lead to a more affordable device, due to the reduction of material employed, unless the design implies a greater burden in maintenance.

A variety of fluid heater modeling tools are available, that emerge from the literature, as genetic algorithm, differential evolution, particle swarm optimization or simulated annealing have become widespread for their application in design and optimization. Campet et al. [15] optimized a single-started helically ribbed HEX by using large eddy simulation, which is based on a surrogate model constructed from Gaussian Process Regression and adaptive resampling with the Efficient Global Optimization (EGO) method. This method can maximize the heat transfer efficiency but has the disadvantage that only is able to compare for the same pumping power, while not has the capacity to compare different flows. Kumar et al. [16] stated that multi objective wale optimization was a suitable method to optimize the constructive parameters of a heater, basing it in decreasing the pressure drop, but could not perform a multivariable analysis. Heater design takes into account many variables, so, a method that can consider all, or at least some of them, would have a better success. With the development of computational technologies, also computational fluid dynamics (CFD) approaches are becoming popular in design and optimization. Still recently, Lofti & Sundén [17] utilized the CFD to qualify a series of internal turbulators in improving the thermo-hydraulic performance of HEXs, for a wide spectrum of possible designs. CFD approaches are indeed attractive for testing the performance of any number of new designs without fabricating prototypes. Pressure and temperature distributions, flow behavior and pattern can be fruitfully explored in any number of virtual scenarios, which gives a huge amount of possibilities and optimizing at several variables at the same time, while the results only differ up to a 1.05% of the experimental ones [18]. For this approach, it is important to note that CFD has also been used for optimize novel designs of HEX, as Bicer et al. [19] optimized the design of a shell-and-tube HEX with novel three-zonal baffle by using ANSYS and the Taguchi method. One alternative to ANSYS is COMSOL Multiphysics, a CFD program based on finite elements that is suited to treat various aspect of the process at once [20].

The present work is aimed to model and optimize the BCET technology as a temperature-sensitive fluid heater. A fully-dimensional thermo-fluid analysis based on CFD, including inherent turbulence, has been implemented corresponding to a preliminary experimental rig. After proper validation with the theoretical temperature increments, the model was effective in determining:

- the variables space of the thermo-fluid dynamic problem;
- effective operation charts to consolidate the knowledge of the thermization performance;
- the ranges of this variable space that lead to heat transfer's uniformity along the active plate, also depending on the inherent fluid dynamic patterns and some common working fluid.

2. Problem formulation

In the present work a prototype of fluid heater based on the BCET technology has been numerically studied. The prototype consisted in a double thermization flow box or control volume (CV), heated by an interspersed active BCET plate (as shown in Fig. 1), connected by means of short PVC branches of 8 mm dia. to a hold-up tank and a circulation pump (not shown). In this configuration, the liquid of given properties is pumped to the CV by means a short inlet pipe, and then out by an outlet pipe at the same side of the CV.

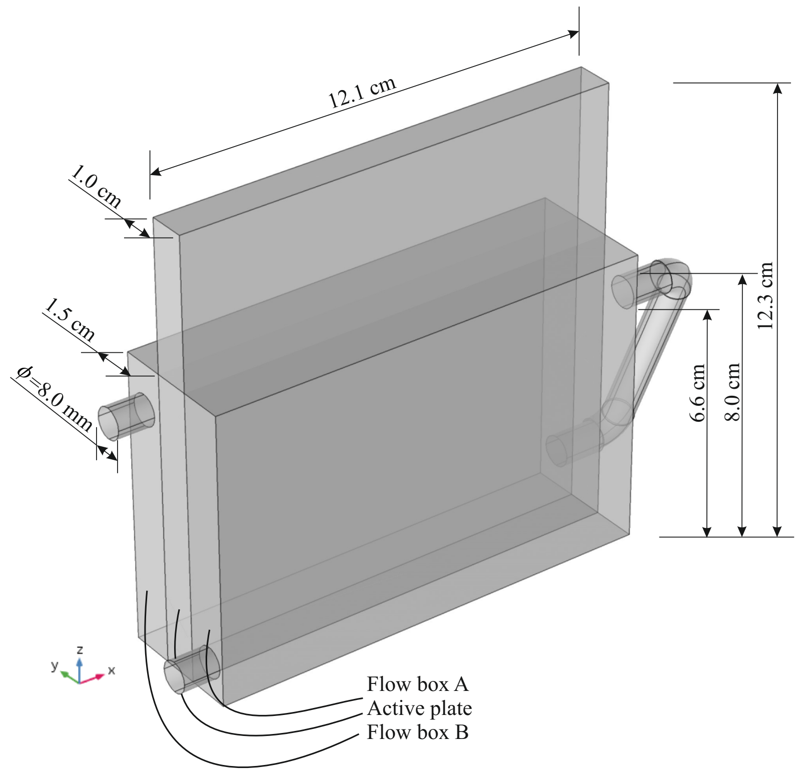

Figure 1: Configuration of the BCET prototype: two flow boxes A and B (including their pipe connections) interspersed by the active plate.

BCET heating is performed by exploiting the ceramic plate properties, i.e. rapidly accumulating heat at before the actual flow circulation, then releasing during flow contact. Details on the experimental rig are reported elsewhere [6]. A typical BCET process is presented in Fig. 2: the MW feed is first turned on, with the flow boxes filled with stagnant fluid, until the desired initial active plate temperature is achieved (in this case, around 100 °C); then the circulation pump is turned on allowing the fluid through the flow boxes. It is evident that, after a short initial transient, with its circulated operation the BCET performs as a single-stream HEX interacting with a constant-power, variable temperature heat sink under a fairly constant temperature difference (15-20 °C in this case). After the desired number of circulation passes p, in the process duration Δt, a final cumulated fluid temperature increase is achieved.

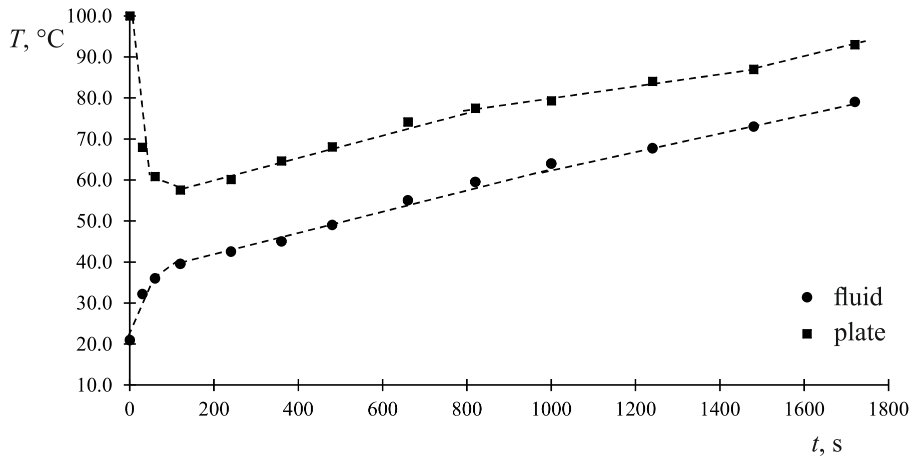

Figure 2: Typical progress of working fluid and plate temperatures.

2.1. *Driving assumptions*

Based on the circulated operation described above, and the small characteristic length of the heat transfer geometry of the heater at stakes (available flow volume divided by active heat transfer surface), a steady-state regime is assumed at each flow pass: the flow field (after a brief start-up transient) does not change during the process and a constant temperature field is established in the fluid.

The following additional assumptions are adopted:

1. The flow is incompressible (negligible pressure work and kinetic energy) with temperature-dependent properties. Due to the adopted flow regime, no body force is accounted for.
2. The viscous heat dissipation is neglected.
3. All non-active wall surfaces are adiabatic.
4. No–slip is enforced at every solid surface.

2.2. *Governing equations*

With reference to the previous statements, the steady-state governing turbulent Reynolds-averaged Navier-Stokes and energy equations are enforced [21], to yield for fluid flow and temperature:

Flow continuity:

$$\nabla \cdot \mathbf{v} = 0 \tag{1}$$

Momentum transfer:

$$\rho \mathbf{v} \cdot \nabla \mathbf{v} = -\nabla p + \nabla \cdot (\mu + \mu_t) \left[\nabla \mathbf{v} + (\nabla \mathbf{v})^{\mathrm{T}} \right] \tag{2}$$

Transfer of turbulent kinetic energy:

$$\rho \mathbf{v} \cdot \nabla k = \nabla \cdot \left[\left(\mu + \frac{\mu_t}{\sigma_k} \right) \nabla k \right] + \frac{\mu_t}{2} \left[\nabla \mathbf{v} + (\nabla \mathbf{v})^{\mathrm{T}} \right]^2 - \rho \varepsilon \tag{3}$$

Transfer of turbulent energy dissipation rate:

$$\rho \mathbf{v} \cdot \nabla \varepsilon = \nabla \cdot \left[\left(\mu + \frac{\mu_t}{\sigma_\varepsilon} \right) \nabla \varepsilon \right] + \frac{c_{1\varepsilon} \varepsilon \mu_t}{2k} \left[\nabla \mathbf{v} + (\nabla \mathbf{v})^{\mathrm{T}} \right]^2 - \frac{c_{2\varepsilon} \rho \varepsilon^2}{k} \tag{4}$$

Transfer of energy:

$$\rho c_p \mathbf{v} \cdot \nabla T = \nabla \cdot (\lambda \nabla T) \tag{5}$$

The present model is based on the $k - \varepsilon$ low-Reynolds turbulence paradigm [22], with its details for turbulent viscosity μ_t and boundary layer at the wall (wall distance initialization) left unreported here for sake of brevity.

2.3. Boundary conditions

With reference to Fig. 3:

- Given conditions at inlet i:

$$v_x = v_{\mathrm{i}}\,, \quad v_y = 0\,, \quad v_z = 0\,, \quad k = k_{\mathrm{i}}\,, \quad \varepsilon = \varepsilon_{\mathrm{i}}\,, \quad T = T_{\mathrm{i}} \tag{6}$$

- At outlet o:

$$\frac{\partial v_x}{\partial x} = 0\,, \quad v_y, v_z = 0\,, \quad \frac{\partial k}{\partial x} = 0\,, \quad \frac{\partial \varepsilon}{\partial x} = 0\,, \quad p = 0\,, \quad \nabla T = 0 \tag{7}$$

- No-slip at all flow box walls:

$$\mathbf{v} = 0 \tag{8}$$

- No heat flux at all flow box walls except the active surface:

$$\nabla T = 0 \tag{9}$$

- Given heat flux at the active surface:

$$\nabla T = \dot{q} \tag{10}$$

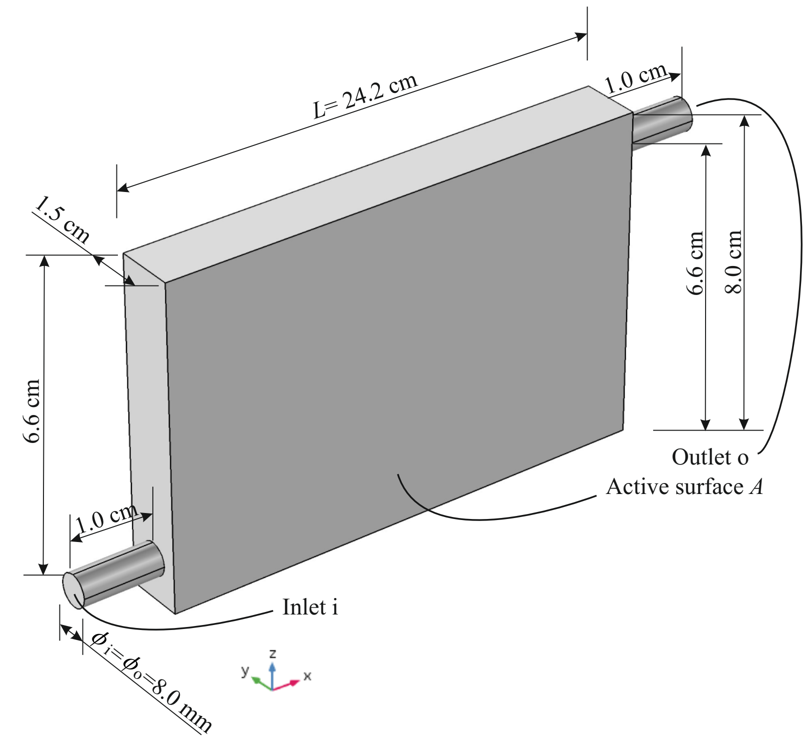

Figure 3: The modified flow box A. Here, an active surface A represents the active plate of Fig. 1.

2.4. Model validation

In order to considerably simplify the flow geometry, while focussing on BCET's nominal exchanged thermal power, one flow box was considered, only, with the total extension of its active heating surface A at the side. In order to do this, flow box A of Fig. 1 was extended to a x-wise length $L = 24.2$ cm, to double surface A with respect to the original design and come up the the geometry in Fig. 3: in this way, a complete fluid/active surface contact for a single flow pass can be simulated.

Since the working fluid is heated by a circulating operation in the BCET, the model of Eqs. (1-9) is solved for the temperature increment of the working fluid $\Delta T_\mathrm{p} = \overline{T}_\mathrm{o} - T_\mathrm{i}$ after a single pass p (with $\overline{T}_\mathrm{o}$ the average of T over outflow section area Ω_o), then multiplying for the total number of passes to yield for the cumulated thermization. Let us refer to an experimental Base Case for water, having supplied a nominal power provided at the active plate $\dot{q}A = 200$ W in a total process duration $\Delta t = 1720$ s. With the total hold-up capacity $V = 1.15$ L and volume flow rate in the flow box $\dot{V} = 2.0$ L/min measured micrometrically, a nominal number of flow passes $\dot{V} \times \Delta t / V = 49.85$ results. Denoting with $\Delta T_\mathrm{p}^\mathrm{v}$ the theoretical temperature increment in the CV, a *control-volume energy conservation balance* for constant fluid specific heat writes as

$$\dot{q}A = \rho\dot{V}c_p\Delta T_\mathrm{p}^\mathrm{v} \tag{11}$$

yielding $\Delta T_\mathrm{p}^\mathrm{v} = 1.43$ °C, which corresponds in a cumulated $\sum_\mathrm{p} \Delta T_\mathrm{p}^\mathrm{v} = \Delta T^\mathrm{v} = 71.28$ °C. In the same conditions, a *control-mass energy conservation balance* applied to the entire BCET rig when holding the corresponding total volume $V = 1.15$ L of water, with a supplied nominal energy $E = \dot{q}A\Delta t = 3.44 \cdot 10^2$ kJ, writes as

$$E = \rho V c_p \Delta T^\mathrm{m} \tag{12}$$

yielding, in the additional assumption of negligible heat loss in the circuit, a cumulated $\Delta T^\mathrm{m} = 71.46$ °C $\simeq \Delta T^\mathrm{v}$. By itself, this agreement confirms the correspondence of the V, $\dot{V}$ and t measurements in the experimental rig, but also gave the opportunity to validate the model. Indeed, in these prescribed conditions, the present BCET model gave a computed temperature increment $\Delta T_\mathrm{p}^\mathrm{c} = 1.36$ °C, yielding a cumulated $\sum_\mathrm{p} \Delta T_\mathrm{p}^\mathrm{c} = \Delta T^\mathrm{c} = 67.80$ °C, corresponding to an error of about 5% with respect to the above theoretical temperature increments.

2.5. *Numerical treatment*

Integration of the partial differential equations system, along with its boundary conditions, was carried out by means of COMSOL [22]. First, the direct MUMPS solver was employed for the wall distance inizialization, with the automatic preordering algorithm and a relative tolerance of $1 \cdot 10^{-3}$; then the direct PARDISO solver with nested multithreaded dissection and a relative tolerance of $1 \cdot 10^{-4}$ was invoked in a segregated fashion with row preordering and multithreaded forward and backward solve, to ensure computational stability and robustness: first for velocity and pressure, then for temperature, and finally for the turbulence parameters. A tetrahedral grid of $109 \cdot 10^3$ total cells has been devised for a Base Case (referred to above) and the geometry of Fig. 3, featuring a boundary layer grid of 4 levels having a thickness of $5 \cdot 10^{-5}$ m, which allowed for resolving the velocity and temperature gradients in the boundary layer, along all solid walls (as an example, see Fig. 4). A grid independency test was carefully performed prior to generation of results by a recursive refinement for both the total cell number and the number and thickness of boundary layer grid levels up to $148 \cdot 10^3$ total cells, with a positive check on $\overline{T}_\mathrm{o}$ (invariance at the 4th meaningful digit) on a $122 \cdot 10^3$ total cells domain, carrying a boundary layer grid of 5 levels having a thickness of $3 \cdot 10^{-5}$ m. The computing time of each run took less than 1 h by using a Pentium Xeon server (Windows 10 OS, Eightcore-32N at 2.4 GHz, 128 GB RAM) running in serial mode.

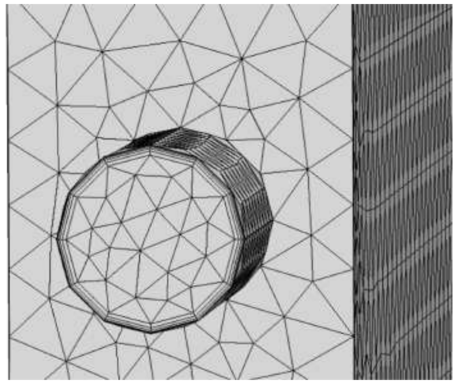

Figure 4: Close-up of the employed finite element grid of Fig. 3, featuring tetrahedral and boundary layer cells, before the flow box inlet. This kind of grid was adopted along all solid walls in the CV.

3. Results and discussion

3.1. Variables space

For a given BCET geometry as in Fig. 1 and with reference to the model in Eqs. (1-9), the governing parameters are the power applied to the active plate $\dot{q}A$ (from 100 to 300 W), the inlet velocity v_{i} (from 0.331 to 1.324 m/s, i.e. a range obtained by scaling the $\dot{V}$ of the Base Case), and the fluid type (water, milk of average characteristics, or common sunflower oil). The variables space have been explored building a full factorial set of computational experiments, for a total of 27 runs. Inlet temperature T_{i} was always kept at 21.00 °C, while the inlet turbulent kinetic energy k_{i} and turbulent energy dissipation rate ϵ_{i} were always consistent with the employed turbulence paradigm. When using the lowest inlet velocity value, model compliance was also checked when using a laminar form of the fluid dynamics, which compared nicely with the turbulent form.

3.2. Operating charts and temperature distributions

Single-pass temperature increases $\Delta T^{\mathrm{c}}_{\mathrm{p}}$ are shown in Fig. 5 for the flow box of Fig. 3, and can be used to implement the desired thermization. Taking into account of the variation of fluid properties with temperature, $\Delta T^{\mathrm{c}}_{\mathrm{p}}$ appears to linearly progress with the increase of the plate power, while depending inversely on the working fluid specific heat and inlet velocity (or mass flow rate). Relative to the Base Case, a full run of 50-pass sequence has been also performed, with the boundary condition of $T_{\mathrm{p,i}} = \iint_{\Omega} T_{\mathrm{p-1,o}}$ at each pass p, to ensure that the cumulated ΔT^{c} does depend linearly on the total number of passes.

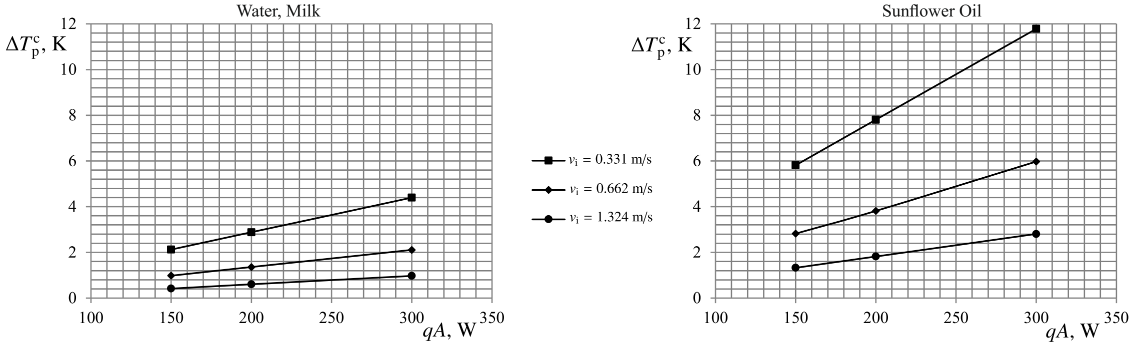

Figure 5: Flow box of Fig. 3: single-pass temperature increases ΔT_p^c charts for the employed fluids, depending on the power applied to the active plate $\dot{q}A$ for variable inlet velocity v_i. Left: Water or Milk; Right: Sunflower Oil.

Qualitative temperature distributions for the flow adjacent to the active plate are shown in Fig. 6, for the three fluids employed. The areas in yellow report on higher temperatures with respect to the various shades of red, representing the departure from an ideal uniform treatment. Water (Left), and milk (Right) to a lesser extent, showed a pronounced circulation pattern at the plate center, and a larger stagnation area corresponding to the upper leading box corner. This pattern is favoured by the dynamic viscosities of these two fluids, that are 1 order-of-magnitude smaller when compared to that of sunflower oil. These areas of uncontrolled, excess temperatures prevent precise thermal control and treatment uniformity at active plate vicinity. As fluid treatment in the heater relies on this thermal contact, the model was therefore used to optimize the single flow box of Fig. 3 in order to promote a more uniform temperature treatment, for the given external dimensions.

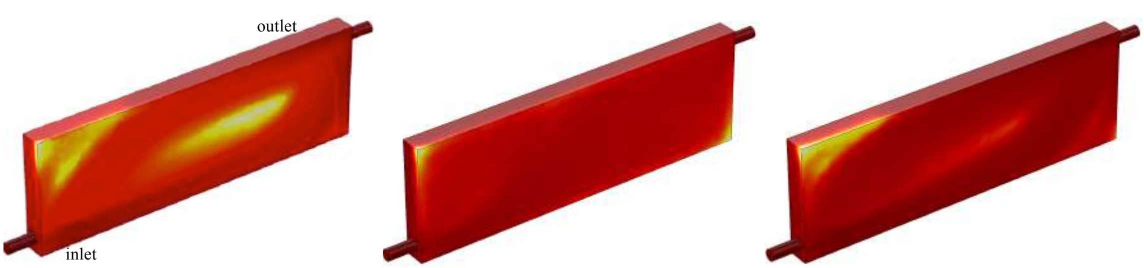

Figure 6: Flow box of Fig. 3: qualitative fluid temperature distributions adjacent to the active plate with L = 24.2 cm, when $\dot{q}A$ = 200 W and v_i = 0.662 m/s (Base Case). Left: Water; Center: Sunflower Oil; Right: Milk. The areas in yellow report on higher temperatures with respect to the various shades of red.

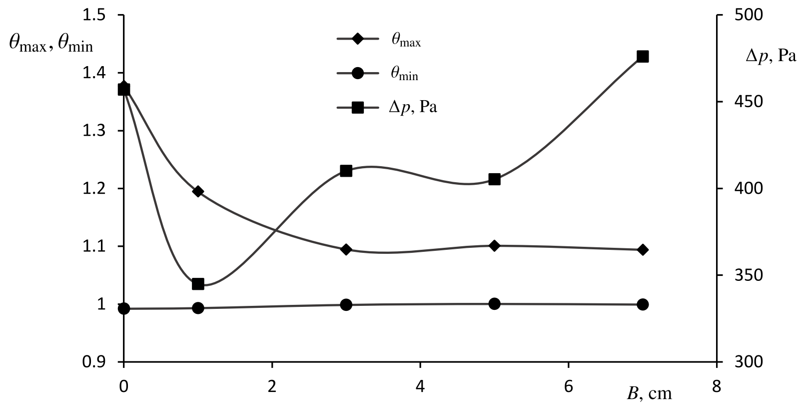

Figure 7: Single flow box of Fig. 1: dimensionless temperatures θ_{max} and θ_{min} at the active plate (left axis), and head loss Δp [Pa] (right axis), as dependent on baffle length B [cm], for the Base Case and milk.

3.3. BCET optimization

When processing many heat-sensitive fluids, the undesired excess/lack temperature levels must be monitored, to ensure for proper quality/safety treatments: too high a temperature may readily spoil some functional feature, such as taste or vitamin content, whereas in turn too low a temperature would hinder the bacterial degradation [23]. Indeed, with the steady-state model at hand, for a given heat transfer characteristic length of the heater, the same amount of energy to the fluid is delivered regardless the internal configuration. In this paper, a simple modification is proposed to optimize the flow boxes of the BCET prototype (Fig. 1), by placing two equidistant thin baffles. Therefore, four additional runs for water in the Base Case were performed, in a parametric loop allowing for various baffle lengths, to compare to the original configuration. These results report on fluid foods, such as milk, that possess similar density and viscosity.

The result of such comparison is reported for the Base Case in Fig. 7. To this end, the fluid maximum and minimum temperatures detected at the vicinity of the plate are compared to the volume average temperature in the CV, to define the following averaging dimensionless temperatures:

$$\theta_{\text{max}} = \frac{T_{\text{max}}}{\iiint_{\text{CV}} T \mathrm{d}V}; \qquad \theta_{\text{min}} = \frac{T_{\text{min}}}{\iiint_{\text{CV}} T \mathrm{d}V} \tag{13}$$

When plotting these θs against the baffle length B, it is evident that no departure of safety treatment is induced in the BCET (the minimum temperatures are kept regardless of B), while uncontrolled thermizations or strong excess temperatures in contact to the active plate will results when using two very short baffles of 1.0 cm, or no baffles at all. In particular, the progress of θ_{max} decreases steadily up to the 3.0 cm-baffle design, then attaining a plateau with varying B.

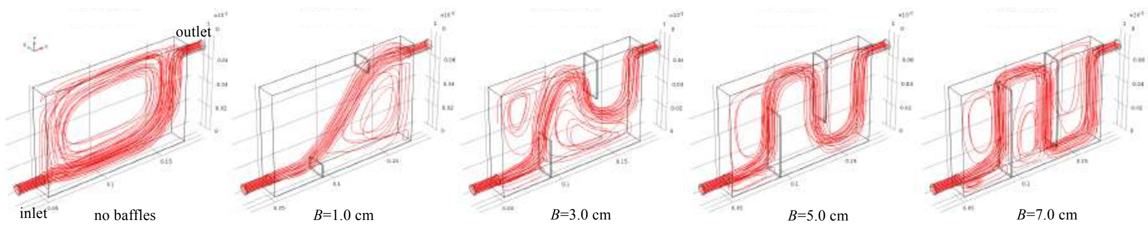

Figure 8: Single flow box of Fig. 1: the velocity field as streamline representation, for the five cases of Fig. 7, at increasing baffle length B. Dimensions are in [m].

At the same time, head loss Δp was also computed and provided in the secondary y-axis of Fig. 7: it is readily seen that the head loss is not linear with the baffle length. By strongly altering the stream patterns (as illustrated in Fig. 8), the baffles' insertion yields two macroscopic effects, in some regions of the CV, whose intensity may vary with length B: smooth deflection of the stream (favorable to a lesser Δp), and relative blocking /impingement of the stream (bringing forth an increase of Δp). The disruption of the single flow cell of the original configuration (with no baffles), when the short baffles with $B = 1.0$ cm are inserted, favors a strong head loss drop (up to 25%) due to the resulting smooth deflection. Then, with increasing B, a 3-cell pattern is formed, but with $B = 3.0$ cm the second baffle (downwind) is long enough to exercise a blocking action on the flow, yielding an increase of 20% in Δp at the end. A longer baffle arrangement ($B = 5.0$ cm) slightly improves the flow deflection, but at the final $B = 7.0$ cm the lateral flow confinement and related head loss is much stronger, and the flow deflection is smooth no more.

Based on these considerations, it is seen that the optimal baffled configuration is the one with 5.0 cm-long baffles. All in all, this configuration allowed to limit the uncontrolled temperature excess by almost 30% ($\theta_{\max}$ dropping from 1.38 to 1.11), while favouring the pressure drop reduction across the flow device by more than 10% (Δp decreasing from 450 to 410).

Temperature plots for some runs reported on in Fig. 7 are also provided in Figs. 9 and 10, by plotting the temperature on the perpendicular axis against the cross-section of the flow box. First, in Fig. 9 the case with no baffles is depicted: it is found a very steep peak of temperature, corresponding to Fig. 6, Left (although now the flow box has a shorter aspect ratio, as in Fig. 3).

When similar plots are provided with internal baffles, as in Fig. 10 against each modified geometry, it is evident how the very short baffles at Left are still insufficient in ensuring a relaxed i.e. more uniform temperature distribution in the vicinity of the plate. The two cases at Center and Right, instead, present more adequate temperature shapes, while the biggest baffle case (7 cm) slightly increases the pressure drop. So,

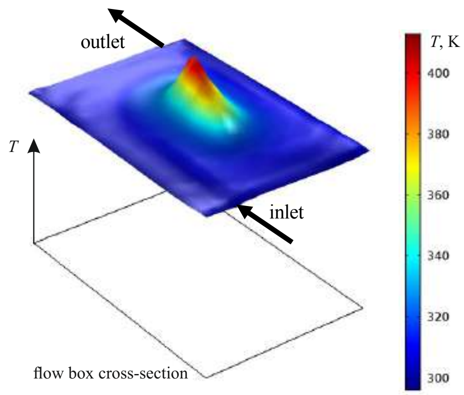

Figure 9: Single flow box of Fig. 1: temperature excess for water and the Base Case, with no baffles, with its scale at right. Inlet and outlet ports' positions are provided.

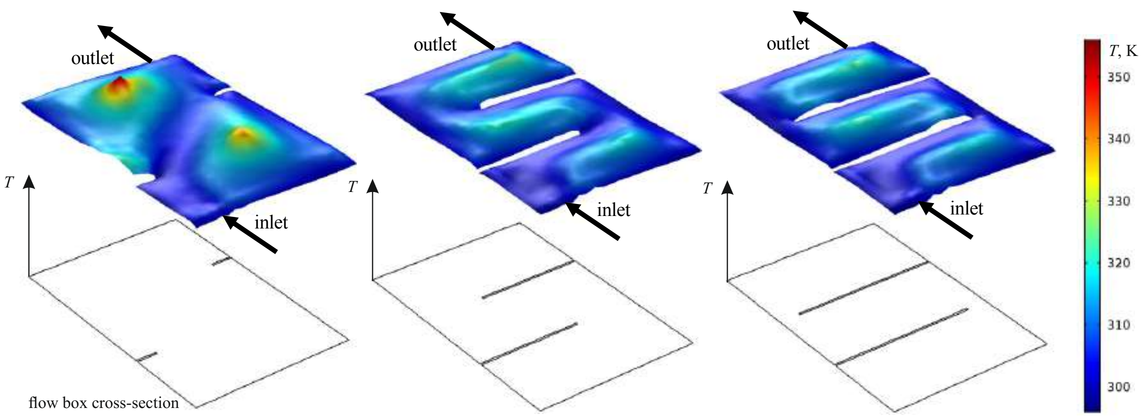

Figure 10: Single flow box of Fig. 1: temperature excess for water and the Base Case, with two 1 cm baffles (Left), two 5 cm baffles (Center), and two 7 cm baffles (Right). The temperature scale is provided at right. Inlet and outlet ports' positions are also provided.

baffles of 5 cm was the chosen option to reduce the overheating while decreasing the pressure drop with its associated increase of efficiency.

Conclusions

In this paper, a prototype of BCET technology was numerically studied and optimized. After validation, the original heater was modelled in 27 different conditions by varying the mass flow rate, the plate power and the fluid type to be heated.

The initial design of the prototype evidenced a pattern of heating inhomogeneity, for fluids that have viscosity and density similar to water. As strong excess temperature could be harmful to fluid features, a new design with different baffle lengths (from 1 to 7 cm) was examined. The optimal length of the baffles was found as 5 cm, which allowed to limit the uncontrolled temperature excess by almost 30%, decrease the difference between the maximum and minimum temperature by about 40%, while favouring the pressure drop reduction across the flow device by more than 10%.

Acknowledgements

This study received funding from the Spanish Ministerio de Economía y Competitividad, Technology Transfer Area, No DI-15-07519.

Author contributions statement

DA conceived the study and developed the analysis, in conjuction with GR. PC and GR developed the computational model and performed the computations, in conjunction with DA. GR wrote the manuscript. All Authors participated in manuscript revisions and discussion, coordinated and critiqued by GR.

Nomenclature

A	active surface area, m^2
B	baffle length, m
$c_{1\varepsilon}$	turbulence model parameter in Eq. (4)
$c_{2\varepsilon}$	turbulence model parameter in Eq. (4)
c_p	constant pressure specific heat, J/kgK
h	specific enthalpy, kJ/kg
k	turbulent kinetic energy, m^2/s^2
L	length, m
p	pressure, Pa
$\dot{q}$	heat flux, W/m^2
t	time, s
T	temperature, K
$\mathbf{v}$	velocity vector, m/s

v velocity component, m/s

$\dot{V}$ volume flow rate, m^3/s

x, y, z coordinates, m

Greek

Δt process duration, s

ΔT temperature increment, K

ε turbulent energy dissipation rate, m^2/s^3

λ thermal conductivity, W/mK

μ dynamic viscosity, Pas

ρ density, kg/m^3

σ_k turbulence model parameter in Eq. (3)

σ_ε turbulence model parameter in Eq. (4)

θ dimensionless temperature

Ω section area, m^2

Subscripts

i inlet

max maximum at the plate

min minimum at the plate

o outlet

p single pass

t turbulent

Superscripts

c computational

m control mass

v control volume

References

[1] Owen, G. (2020). What makes climate change adaptation effective? A systematic review of the literature. Global Environmental Change, 62, 102071.

[2] Ladha-Sabur, A., Bakalis, S., Fryer, P. J., & Lopez-Quiroga, E. (2019). Mapping energy consumption in food manufacturing. Trends in Food Science & Technology, 86, 270-280.

[3] Makroo, H. A., Rastogi, N. K., & Srivastava, B. (2020). Ohmic heating assisted inactivation of enzymes and microorganisms in foods: A review. Trends in Food Science & Technology.

[4] Roberts, P. B. (2016). Food irradiation: Standards, regulations and world-wide trade. Radiation Physics and Chemistry, 129, 30-34.

[5] Ekezie, F. G. C., Sun, D. W., Han, Z., & Cheng, J. H. (2017). Microwave-assisted food processing technologies for enhancing product quality and process efficiency A review of recent developments. Trends in Food Science & Technology, 67, 58-69.

[6] Fernandez, J., Reyes-Davo, E., Reyes-Canovas, R., Garcia-Sevilla, J., Vela-Carrascosa, E., & Jara-Rico, A. (2015). Heating cell, heater using same, heating system and use thereof. ES2568749; PCT/ES, 70712, 2015.

[7] Fellows, P. J. (2009). Food processing technology: principles and practice, Chapter 8 p. 520. Elsevier.

[8] Deeth, H. C., & Lewis, M. J. (2017). High temperature processing of milk and milk products. John Wiley & Sons.

[9] Agcam, E., Akyildiz, A., & Dundar, B. (2018). Thermal pasteurization and microbial inactivation of fruit juices. In Fruit Juices (pp. 309-339). Academic Press.

[10] Zhang, Y., & Ma, H. B. (2008). Nonequilibrium heat conduction in a nanofluid layer with periodic heat flux. International journal of heat and mass transfer, 51(19-20), 4862-4874.

[11] Yang, J., Oh, S. R., & Liu, W. (2014). Optimization of shell-and-tube heat exchangers using a general design approach motivated by constructal theory. International Journal of heat and mass transfer, 77, 1144-1154.

[12] Picon-Nuñez, M., Polley, G. T., & Martinez-Rodriguez, G. (2013). Graphical tool for the preliminary design of compact heat exchangers. Applied thermal engineering, 61(1), 36-43.

[13] Caputo, A. C., Pelagagge, P. M., & Salini, P. (2008). Heat exchanger design based on economic optimisation. Applied thermal engineering, 28(10), 1151-1159.

[14] Ricci, R., Romagnoli, R., Montelpare, S., & Di Benedetto, D. (2014). Convective heat transfer increase in internal laminar flow using a vibrating surface. International journal of thermal sciences, 84, 358-368.

[15] Campet, R., Roy, P. T., Cuenot, B., Riber, E., & Jouhaud, J. C. (2020). Design optimization of an heat exchanger using Gaussian process. International Journal of Heat and Mass Transfer, 150, 119264.

[16] Kumar, S.D., Chandramohan, D., Purushothaman, K.,& Sathish, T., (2020). Optimal hydraulic and thermal constrain for plate heat exchanger using multi objective wale optimization. Materials Today Proceedings, 21, 876-881.

[17] Lofti, B., & Sundén, B. (2020). Thermo-hydraulic performance enhancement of finned elliptical tube heat exchangers by utilizing innovative dimple turbulators. Heat Transfer Engineering, 41, 1117-1142.

[18] Abeykoon, C. (2020). Compact heat exchangers design and optimization with CFD. International Journal of Heat and Mass Transfer, 146, 118766.

[19] Bicer, N., Engin, T., Yasar, H., Buyukkaya, E., & Aydin, A. (2020). Design optimization of a shell-and-tube heat exchanger with novel three-zonal baffle by using CFD and taguchi method. International Journal of Thermal Sciences, 155, 106417.

[20] Pepper, D. W., & Heinrich, J. C. (2017). The finite element method: basic concepts and applications with MATLAB, MAPLE, and COMSOL. CRC press.

[21] Ruocco, G. (2018). Introduction to Transport Phenomena Modeling: A Multiphysics, General Equation-Based Approach, pp. 106 and 166. Springer.

[22] COMSOL Multiphysics (2018) v. 5.2a. www.comsol.com. COMSOL AB, Stockholm, Sweden.

[23] Toledo, R. T., Singh, R. K., & Kong, F. (2007). Fundamentals of food process engineering, pp. 211. Springer.

Manuscript File
Click here to view linked References

Optimal design of an innovative microwave-based fluid heater

Diego Alcañiz[a], Paolo Caccavale[b], Maria Valeria De Bonis[b], Ruth de los Reyes[a], Maria Dolores Ortolá[a], Gianpaolo Ruocco[b,*]

[a]*Instituto Universitario de Ingenieria de Alimentos para el Desarrollo, Universitat Politècnica de València, Camino de Vera s/n, 46022 Valencia, Spain*
[b]*Scuola d'Ingegneria, Università degli Studi della Basilicata Campus Macchia Romana, 85100 Potenza, Italy*

Abstract

New heating technologies are constantly being developed worldwide, specially the electrical ones that take advantage of renewable energy. In this paper, the Basic Cell of Energy Transference (BCET) is proposed as an innovative fluid heater, carrying a microwave-fed heat transfer plate for thermal contact. A fully-dimensional thermo-fluid analysis was implemented and validated to determine the key design parameters and operation features for heat transfer to temperature-sensitive working fluids.

Circulation patterns were observed, when using certain fluids, in turn causing strong temperature non-uniformities. As fluid treatment in the heater relies on the thermal contact at its active plate, the model was used to ascertain the undesired excess/lack temperature range for quality/safety treatments, with reference to a final effective process temperature. Therefore, a geometry optimization by means of internal baffles was carried out which ensured variation to fluid pattern and more uniform active plate temperature. In a base case, the new design allowed to limit the uncontrolled temperature excess by almost 30%, while favouring the pressure drop reduction across the flow device by more than 10%.

Keywords: Fluid Heater, Computational Fluid Dynamics, Heat transfer and fluid dynamics optimization

1. Introduction

Nowadays, new heating technologies are being developed all around the world, specially, technologies that can be feed with electricity. Over the past two decades, rapid growth in the development of adaptation responses to climate change has occurred around the world [1]. Therefore, the interest in the electrical-feed heating in common processes (such as in the food industry) has risen considerably as it can take advantage

*Corresponding author
Email address: `gianpaolo.ruocco@unibas.it` (Gianpaolo Ruocco)

of renewable sources of energy, and as it has far less associated CO_2 emissions than the fossil fuels technologies. Process heating is an area of interest for emission reduction as the 70% of the total energy cost of some sectors of the food industry comes from heating processes [2].

There are many novel technologies that can be used for heating applications and, specifically, to heat liquids, like ohmic heating [3], irradiation [4] or microwave (MW)[5]. One such example is the Basic Cell of Energy Transference (BCET) [6], which consists, in its simplest configuration, in two flow boxes interspersed by an active heat transfer plate. The working fluid flows sequentially through the two box, making thermal contact with the active ceramic plate, which is heated by conducted MW. Due to its specifically-designed composition and dimensions, optimized to absorb MW, the active part of the BCET provides precise, efficient and flexible operation to heat fluids in a similar way than a Plate Heat Exchanger (HEX) the most widespread device for heating fluids industrially [7]. Thanks to its compact design and working simplicity (no auxiliary fluid is necessary), it finds its application for precise liquid thermization and in rural areas installations, that can benefit of solar- or wind-driven energy and cannot depend upon a regular water supply. Its feeding technology allows for precise hold-up times, e.g. for pasteurization processes [8, 9] and finely-tuned power modulation from the active plate, e.g. with oscillating/periodic heat flux as in nanofluids thermization [10], which requires more immediate response to temperature changes.

HEX and heater design optimization is a very active area of research an development. Recently, Yang et al. [11], Picon-Nuñez et al. [12], Caputo et al. [13] confirmed that the pressure drop is correlated with the heat transfer coefficient, which is the key concept at stake here. While higher heat transfer contact and removal from the heater's active plate (or heater efficiency) is ensured by turbulent flow conditions, laminar flows are preferred instead to decrease the cost associated with pumping power [14]. On the other hand, the increment of heater efficiency, for a given active surface area, may lead to a more affordable device, due to the reduction of material employed, unless the design implies a greater burden in maintenance.

A variety of fluid heater modeling tools are available, that emerge from the literature, as genetic algorithm, differential evolution, particle swarm optimization or simulated annealing have become widespread for their application in design and optimization. Campet et al. [15] optimized a single-started helically ribbed HEX by using large eddy simulation, which is based on a surrogate model constructed from Gaussian Process Regression and adaptive resampling with the Efficient Global Optimization (EGO) method. This method can maximize the heat transfer efficiency but has the disadvantage that only is able to compare for the same pumping power, while not has the capacity to compare different flows. Kumar et al. [16] stated that multi objective wale optimization was a suitable method to optimize the constructive parameters of a heater, basing it in decreasing the pressure drop, but could not perform a multivariable analysis. Heater design takes into account many variables, so, a method that can consider all, or at least some of them, would have a better success. With the development of computational technologies, also computational fluid dynamics (CFD) approaches are becoming popular in design and optimization. Still recently, Lofti & Sundén [17] utilized the CFD to qualify a series of internal turbulators in improving the thermo-hydraulic performance of HEXs, for a wide spectrum of possible designs. CFD approaches are indeed attractive for testing the performance of any number of new designs without fabricating prototypes. Pressure and temperature distributions, flow behavior and pattern can be fruitfully explored in any number of virtual scenarios, which gives a huge amount of possibilities and optimizing at several variables at the same time, while the results only differ up to a 1.05% of the experimental ones [18]. For this approach, it is important to note that CFD has also been used for optimize novel designs of HEX, as Bicer et al. [19] optimized the design of a shell-and-tube HEX with novel three-zonal baffle by using ANSYS and the Taguchi method. One alternative to ANSYS is COMSOL Multiphysics, a CFD program based on finite elements that is suited to treat various aspect of the process at once [20].

The present work is aimed to model and optimize the BCET technology as a temperature-sensitive fluid heater. A fully-dimensional thermo-fluid analysis based on CFD, including inherent turbulence, has been implemented corresponding to a preliminary experimental rig. After proper validation with the theoretical temperature increments, the model was effective in determining:

- the variables space of the thermo-fluid dynamic problem;
- effective operation charts to consolidate the knowledge of the thermization performance;
- the ranges of this variable space that lead to heat transfer's uniformity along the active plate, also depending on the inherent fluid dynamic patterns and some common working fluid.

2. Problem formulation

In the present work a prototype of fluid heater based on the BCET technology has been numerically studied. The prototype consisted in a double thermization flow box or control volume (CV), heated by an interspersed active BCET plate (as shown in Fig. 1), connected by means of short PVC branches of 8 mm dia. to a hold-up tank and a circulation pump (not shown). In this configuration, the liquid of given properties is pumped to the CV by means a short inlet pipe, and then out by an outlet pipe at the same side of the CV.

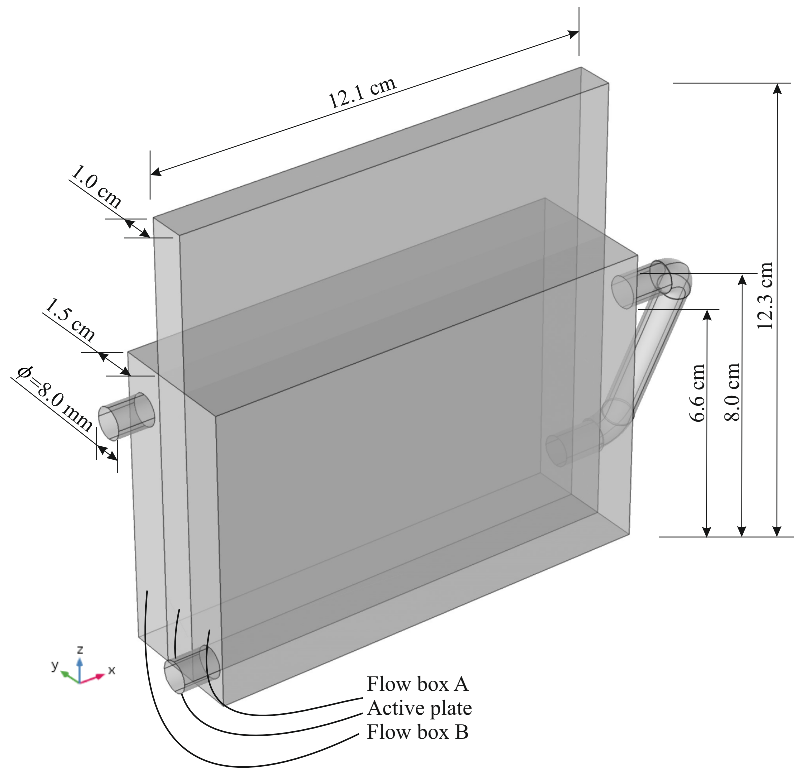

Figure 1: Configuration of the BCET prototype: two flow boxes A and B (including their pipe connections) interspersed by the active plate.

BCET heating is performed by exploiting the ceramic plate properties, i.e. rapidly accumulating heat at before the actual flow circulation, then releasing during flow contact. Details on the experimental rig are reported elsewhere [6]. A typical BCET process is presented in Fig. 2: the MW feed is first turned on, with the flow boxes filled with stagnant fluid, until the desired initial active plate temperature is achieved (in this case, around 100 °C); then the circulation pump is turned on allowing the fluid through the flow boxes. It is evident that, after a short initial transient, with its circulated operation the BCET performs as a single-stream HEX interacting with a constant-power, variable temperature heat sink under a fairly constant temperature difference (15-20 °C in this case). After the desired number of circulation passes p, in the process duration Δt, a final cumulated fluid temperature increase is achieved.

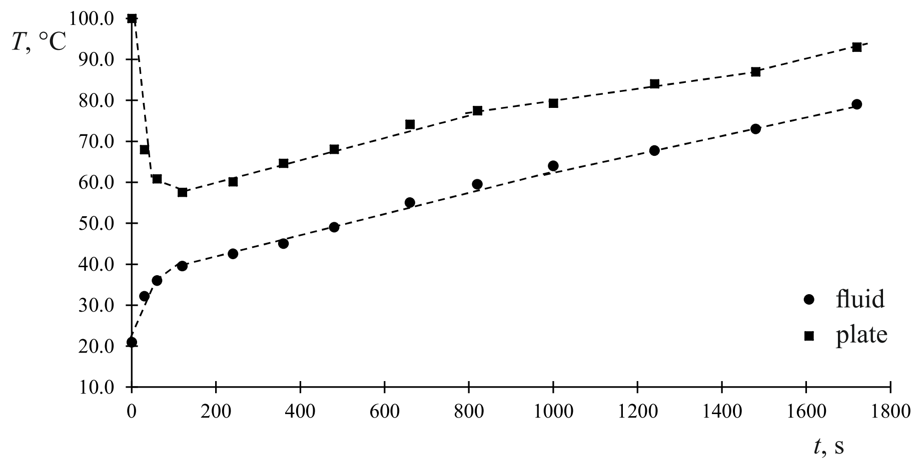

Figure 2: Typical progress of working fluid and plate temperatures.

2.1. *Driving assumptions*

Based on the circulated operation described above, and the small characteristic length of the heat transfer geometry of the heater at stakes (available flow volume divided by active heat transfer surface), a steady-state regime is assumed at each flow pass: the flow field (after a brief start-up transient) does not change during the process and a constant temperature field is established in the fluid.

The following additional assumptions are adopted:

1. The flow is incompressible (negligible pressure work and kinetic energy) with temperature-dependent properties. Due to the adopted flow regime, no body force is accounted for.
2. The viscous heat dissipation is neglected.
3. All non-active wall surfaces are adiabatic.
4. No–slip is enforced at every solid surface.

2.2. *Governing equations*

With reference to the previous statements, the steady-state governing turbulent Reynolds-averaged Navier-Stokes and energy equations are enforced [21], to yield for fluid flow and temperature:

Flow continuity:

$$\nabla \cdot \mathbf{v} = 0 \tag{1}$$

Momentum transfer:

$$\rho \mathbf{v} \cdot \nabla \mathbf{v} = -\nabla p + \nabla \cdot (\mu + \mu_t) \left[\nabla \mathbf{v} + (\nabla \mathbf{v})^{\mathrm{T}} \right] \tag{2}$$

Transfer of turbulent kinetic energy:

$$\rho \mathbf{v} \cdot \nabla k = \nabla \cdot \left[\left(\mu + \frac{\mu_t}{\sigma_k} \right) \nabla k \right] + \frac{\mu_t}{2} \left[\nabla \mathbf{v} + (\nabla \mathbf{v})^{\mathrm{T}} \right]^2 - \rho \varepsilon \tag{3}$$

Transfer of turbulent energy dissipation rate:

$$\rho \mathbf{v} \cdot \nabla \varepsilon = \nabla \cdot \left[\left(\mu + \frac{\mu_t}{\sigma_\varepsilon} \right) \nabla \varepsilon \right] + \frac{c_{1\varepsilon} \varepsilon \mu_t}{2k} \left[\nabla \mathbf{v} + (\nabla \mathbf{v})^{\mathrm{T}} \right]^2 - \frac{c_{2\varepsilon} \rho \varepsilon^2}{k} \tag{4}$$

Transfer of energy:

$$\rho c_p \mathbf{v} \cdot \nabla T = \nabla \cdot (\lambda \nabla T) \tag{5}$$

The present model is based on the $k - \varepsilon$ low-Reynolds turbulence paradigm [22], with its details for turbulent viscosity μ_t and boundary layer at the wall (wall distance initialization) left unreported here for sake of brevity.

2.3. Boundary conditions

With reference to Fig. 3:

- Given conditions at inlet i:

$$v_x = v_\mathrm{i}\,, \quad v_y = 0\,, \quad v_z = 0\,, \quad k = k_\mathrm{i}\,, \quad \varepsilon = \varepsilon_\mathrm{i}\,, \quad T = T_\mathrm{i} \tag{6}$$

- At outlet o:

$$\frac{\partial v_x}{\partial x} = 0\,, \quad v_y, v_z = 0\,, \quad \frac{\partial k}{\partial x} = 0\,, \quad \frac{\partial \varepsilon}{\partial x} = 0\,, \quad p = 0\,, \quad \nabla T = 0 \tag{7}$$

- No-slip at all flow box walls:

$$\mathbf{v} = 0 \tag{8}$$

- No heat flux at all flow box walls except the active surface:

$$\nabla T = 0 \tag{9}$$

- Given heat flux at the active surface:

$$\nabla T = \dot{q} \tag{10}$$

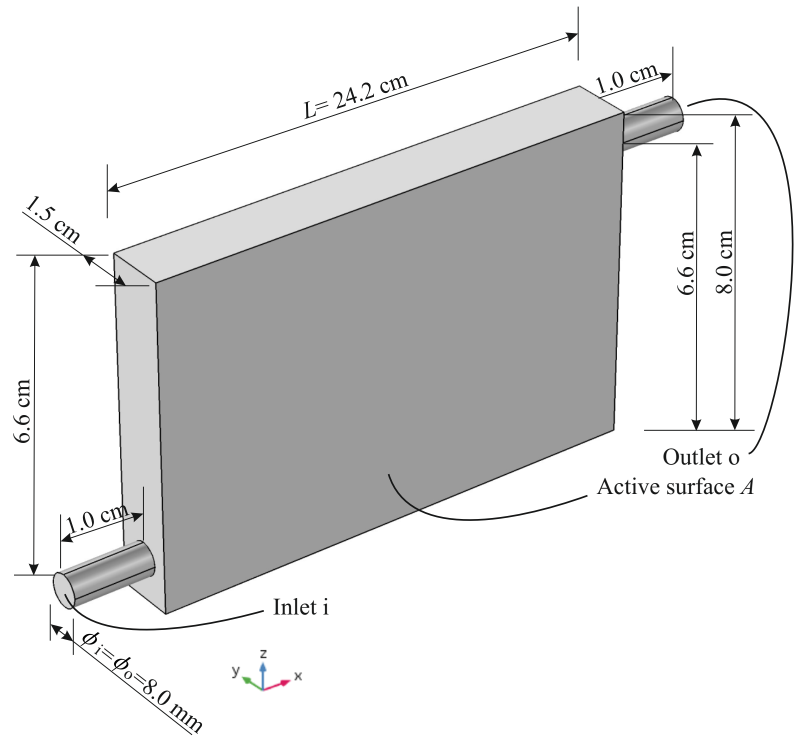

Figure 3: The modified flow box A. Here, an active surface A represents the active plate of Fig. 1.

2.4. *Model validation*

In order to considerably simplify the flow geometry, while focussing on BCET's nominal exchanged thermal power, one flow box was considered, only, with the total extension of its active heating surface A at the side. In order to do this, flow box A of Fig. 1 was extended to a x-wise length $L = 24.2$ cm, to double surface A with respect to the original design and come up the the geometry in Fig. 3: in this way, a complete fluid/active surface contact for a single flow pass can be simulated.

Since the working fluid is heated by a circulating operation in the BCET, the model of Eqs. (1-9) is solved for the temperature increment of the working fluid $\Delta T_{\mathrm{p}} = \overline{T}_{\mathrm{o}} - T_{\mathrm{i}}$ after a single pass p (with $\overline{T}_{\mathrm{o}}$ the average of T over outflow section area Ω_{o}), then multiplying for the total number of passes to yield for the cumulated thermization. Let us refer to an experimental Base Case for water, having supplied a nominal power provided at the active plate $\dot{q}A = 200$ W in a total process duration $\Delta t = 1720$ s. With the total hold-up capacity $V = 1.15$ L and volume flow rate in the flow box $\dot{V} = 2.0$ L/min measured micrometrically, a nominal number of flow passes $\dot{V} \times \Delta t / V = 49.85$ results. Denoting with $\Delta T_{\mathrm{p}}^{\mathrm{v}}$ the theoretical temperature increment in the CV, a *control-volume energy conservation balance* for constant fluid specific heat writes as

$$\dot{q}A = \rho\dot{V}c_p\Delta T_\mathrm{p}^\mathrm{v} \tag{11}$$

yielding $\Delta T_\mathrm{p}^\mathrm{v} = 1.43$ °C, which corresponds in a cumulated $\sum_\mathrm{p}\Delta T_\mathrm{p}^\mathrm{v} = \Delta T^\mathrm{v} = 71.28$ °C. In the same conditions, a *control-mass energy conservation balance* applied to the entire BCET rig when holding the corresponding total volume $V = 1.15$ L of water, with a supplied nominal energy $E = \dot{q}A\Delta t = 3.44 \cdot 10^2$ kJ, writes as

$$E = \rho V c_p \Delta T^\mathrm{m} \tag{12}$$

yielding, in the additional assumption of negligible heat loss in the circuit, a cumulated $\Delta T^\mathrm{m} = 71.46$ °C $\simeq \Delta T^\mathrm{v}$. By itself, this agreement confirms the correspondence of the V, $\dot{V}$ and t measurements in the experimental rig, but also gave the opportunity to validate the model. Indeed, in these prescribed conditions, the present BCET model gave a computed temperature increment $\Delta T_\mathrm{p}^\mathrm{c} = 1.36$ °C, yielding a cumulated $\sum_\mathrm{p}\Delta T_\mathrm{p}^\mathrm{c} = \Delta T^\mathrm{c} = 67.80$ °C, corresponding to an error of about 5% with respect to the above theoretical temperature increments.

2.5. Numerical treatment

Integration of the partial differential equations system, along with its boundary conditions, was carried out by means of COMSOL [22]. First, the direct MUMPS solver was employed for the wall distance inizialization, with the automatic preordering algorithm and a relative tolerance of $1 \cdot 10^{-3}$; then the direct PARDISO solver with nested multithreaded dissection and a relative tolerance of $1 \cdot 10^{-4}$ was invoked in a segregated fashion with row preordering and multithreaded forward and backward solve, to ensure computational stability and robustness: first for velocity and pressure, then for temperature, and finally for the turbulence parameters. A tetrahedral grid of $109 \cdot 10^3$ total cells has been devised for a Base Case (referred to above) and the geometry of Fig. 3, featuring a boundary layer grid of 4 levels having a thickness of $5 \cdot 10^{-5}$ m, which allowed for resolving the velocity and temperature gradients in the boundary layer, along all solid walls (as an example, see Fig. 4). A grid independency test was carefully performed prior to generation of results by a recursive refinement for both the total cell number and the number and thickness of boundary layer grid levels up to $148 \cdot 10^3$ total cells, with a positive check on $\overline{T}_\mathrm{o}$ (invariance at the 4th meaningful digit) on a $122 \cdot 10^3$ total cells domain, carrying a boundary layer grid of 5 levels having a thickness of $3 \cdot 10^{-5}$ m. The computing time of each run took less than 1 h by using a Pentium Xeon server (Windows 10 OS, Eightcore-32N at 2.4 GHz, 128 GB RAM) running in serial mode.

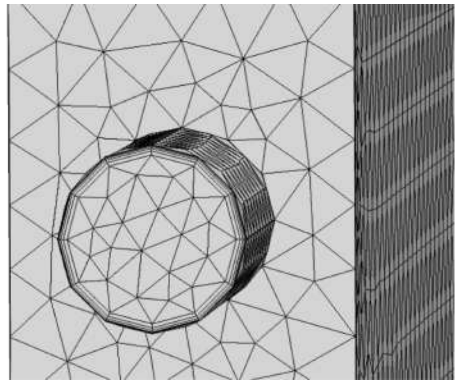

Figure 4: Close-up of the employed finite element grid of Fig. 3, featuring tetrahedral and boundary layer cells, before the flow box inlet. This kind of grid was adopted along all solid walls in the CV.

3. Results and discussion

3.1. Variables space

For a given BCET geometry as in Fig. 1 and with reference to the model in Eqs. (1-9), the governing parameters are the power applied to the active plate $\dot{q}A$ (from 100 to 300 W), the inlet velocity v_{i} (from 0.331 to 1.324 m/s, i.e. a range obtained by scaling the $\dot{V}$ of the Base Case), and the fluid type (water, milk of average characteristics, or common sunflower oil). The variables space have been explored building a full factorial set of computational experiments, for a total of 27 runs. Inlet temperature T_{i} was always kept at 21.00 °C, while the inlet turbulent kinetic energy k_{i} and turbulent energy dissipation rate ϵ_{i} were always consistent with the employed turbulence paradigm. When using the lowest inlet velocity value, model compliance was also checked when using a laminar form of the fluid dynamics, which compared nicely with the turbulent form.

3.2. Operating charts and temperature distributions

Single-pass temperature increases $\Delta T_{\mathrm{p}}^{\mathrm{c}}$ are shown in Fig. 5 for the flow box of Fig. 3, and can be used to implement the desired thermization. Taking into account of the variation of fluid properties with temperature, $\Delta T_{\mathrm{p}}^{\mathrm{c}}$ appears to linearly progress with the increase of the plate power, while depending inversely on the working fluid specific heat and inlet velocity (or mass flow rate). Relative to the Base Case, a full run of 50-pass sequence has been also performed, with the boundary condition of $T_{\mathrm{p,i}} = \iint_{\Omega} T_{\mathrm{p-1,o}}$ at each pass p, to ensure that the cumulated ΔT^{c} does depend linearly on the total number of passes.

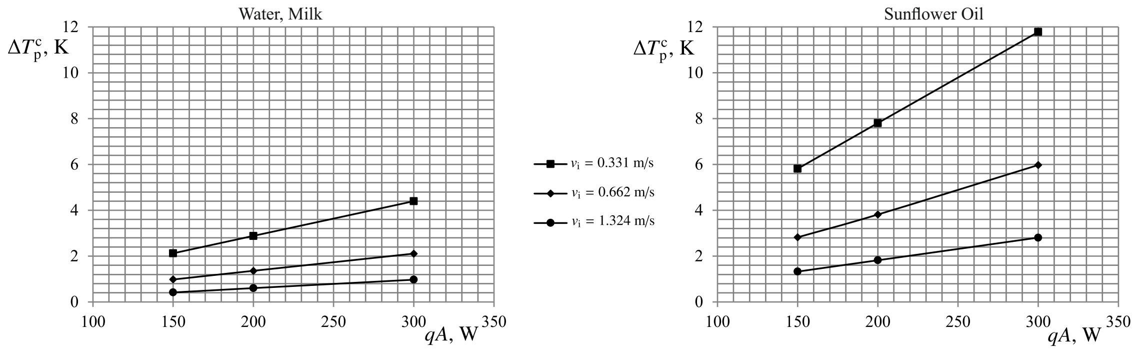

Figure 5: Flow box of Fig. 3: single-pass temperature increases ΔT_p^c charts for the employed fluids, depending on the power applied to the active plate $\dot{q}A$ for variable inlet velocity v_i. Left: Water or Milk; Right: Sunflower Oil.

Qualitative temperature distributions for the flow adjacent to the active plate are shown in Fig. 6, for the three fluids employed. The areas in yellow report on higher temperatures with respect to the various shades of red, representing the departure from an ideal uniform treatment. Water (Left), and milk (Right) to a lesser extent, showed a pronounced circulation pattern at the plate center, and a larger stagnation area corresponding to the upper leading box corner. This pattern is favoured by the dynamic viscosities of these two fluids, that are 1 order-of-magnitude smaller when compared to that of sunflower oil. These areas of uncontrolled, excess temperatures prevent precise thermal control and treatment uniformity at active plate vicinity. As fluid treatment in the heater relies on this thermal contact, the model was therefore used to optimize the single flow box of Fig. 3 in order to promote a more uniform temperature treatment, for the given external dimensions.

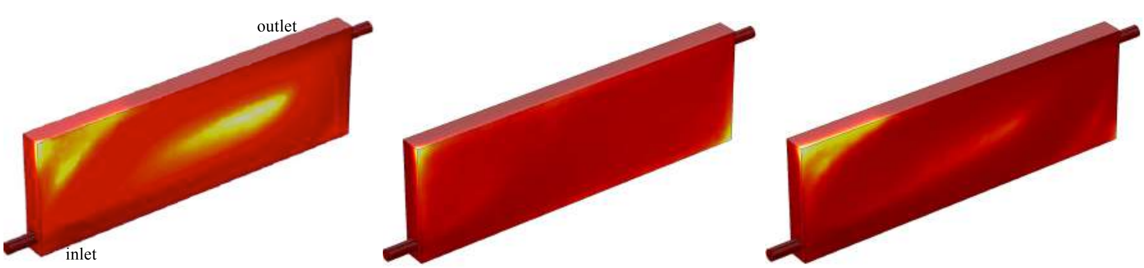

Figure 6: Flow box of Fig. 3: qualitative fluid temperature distributions adjacent to the active plate with L = 24.2 cm, when $\dot{q}A$ = 200 W and v_i = 0.662 m/s (Base Case). Left: Water; Center: Sunflower Oil; Right: Milk. The areas in yellow report on higher temperatures with respect to the various shades of red.

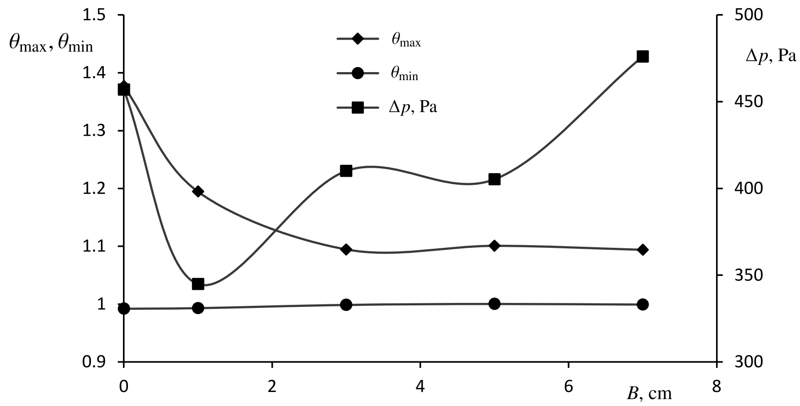

Figure 7: Single flow box of Fig. 1: dimensionless temperatures θ_{max} and θ_{min} at the active plate (left axis), and head loss Δp [Pa] (right axis), as dependent on baffle length B [cm], for the Base Case and milk.

3.3. BCET optimization

When processing many heat-sensitive fluids, the undesired excess/lack temperature levels must be monitored, to ensure for proper quality/safety treatments: too high a temperature may readily spoil some functional feature, such as taste or vitamin content, whereas in turn too low a temperature would hinder the bacterial degradation [23]. Indeed, with the steady-state model at hand, for a given heat transfer characteristic length of the heater, the same amount of energy to the fluid is delivered regardless the internal configuration. In this paper, a simple modification is proposed to optimize the flow boxes of the BCET prototype (Fig. 1), by placing two equidistant thin baffles. Therefore, four additional runs for water in the Base Case were performed, in a parametric loop allowing for various baffle lengths, to compare to the original configuration. These results report on fluid foods, such as milk, that possess similar density and viscosity.

The result of such comparison is reported for the Base Case in Fig. 7. To this end, the fluid maximum and minimum temperatures detected at the vicinity of the plate are compared to the volume average temperature in the CV, to define the following averaging dimensionless temperatures:

$$\theta_{max} = \frac{T_{max}}{\iiint_{CV} T \mathrm{d}V}; \qquad \theta_{min} = \frac{T_{min}}{\iiint_{CV} T \mathrm{d}V} \tag{13}$$

When plotting these θs against the baffle length B, it is evident that no departure of safety treatment is induced in the BCET (the minimum temperatures are kept regardless of B), while uncontrolled thermizations or strong excess temperatures in contact to the active plate will results when using two very short baffles of 1.0 cm, or no baffles at all. In particular, the progress of θ_{max} decreases steadily up to the 3.0 cm-baffle design, then attaining a plateau with varying B.

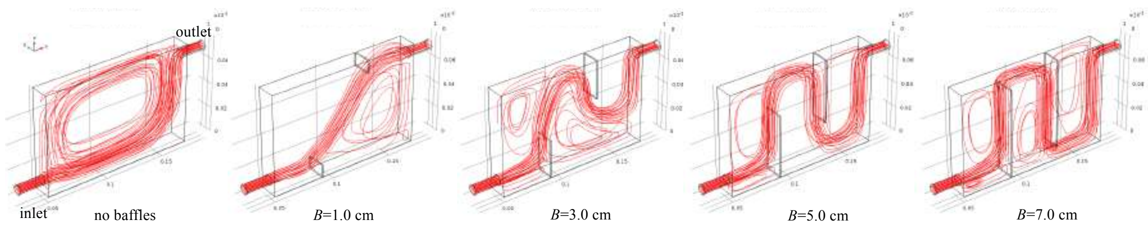

Figure 8: Single flow box of Fig. 1: the velocity field as streamline representation, for the five cases of Fig. 7, at increasing baffle length B. Dimensions are in [m].

At the same time, head loss Δp was also computed and provided in the secondary y-axis of Fig. 7: it is readily seen that the head loss is not linear with the baffle length. By strongly altering the stream patterns (as illustrated in Fig. 8), the baffles' insertion yields two macroscopic effects, in some regions of the CV, whose intensity may vary with length B: smooth deflection of the stream (favorable to a lesser Δp), and relative blocking /impingement of the stream (bringing forth an increase of Δp). The disruption of the single flow cell of the original configuration (with no baffles), when the short baffles with $B = 1.0$ cm are inserted, favors a strong head loss drop (up to 25%) due to the resulting smooth deflection. Then, with increasing B, a 3-cell pattern is formed, but with $B = 3.0$ cm the second baffle (downwind) is long enough to exercise a blocking action on the flow, yielding an increase of 20% in Δp at the end. A longer baffle arrangement ($B = 5.0$ cm) slightly improves the flow deflection, but at the final $B = 7.0$ cm the lateral flow confinement and related head loss is much stronger, and the flow deflection is smooth no more.

Based on these considerations, it is seen that the optimal baffled configuration is the one with 5.0 cm-long baffles. All in all, this configuration allowed to limit the uncontrolled temperature excess by almost 30% ($\theta_{\max}$ dropping from 1.38 to 1.11), while favouring the pressure drop reduction across the flow device by more than 10% (Δp decreasing from 450 to 410).

Temperature plots for some runs reported on in Fig. 7 are also provided in Figs. 9 and 10, by plotting the temperature on the perpendicular axis against the cross-section of the flow box. First, in Fig. 9 the case with no baffles is depicted: it is found a very steep peak of temperature, corresponding to Fig. 6, Left (although now the flow box has a shorter aspect ratio, as in Fig. 3).

When similar plots are provided with internal baffles, as in Fig. 10 against each modified geometry, it is evident how the very short baffles at Left are still insufficient in ensuring a relaxed i.e. more uniform temperature distribution in the vicinity of the plate. The two cases at Center and Right, instead, present more adequate temperature shapes, while the biggest baffle case (7 cm) slightly increases the pressure drop. So,

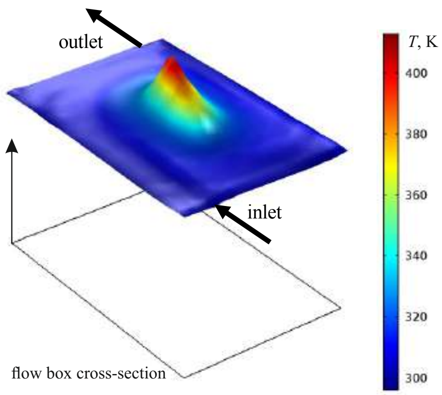

Figure 9: Single flow box of Fig. 1: temperature excess for water and the Base Case, with no baffles, with its scale at right. Inlet and outlet ports' positions are provided.

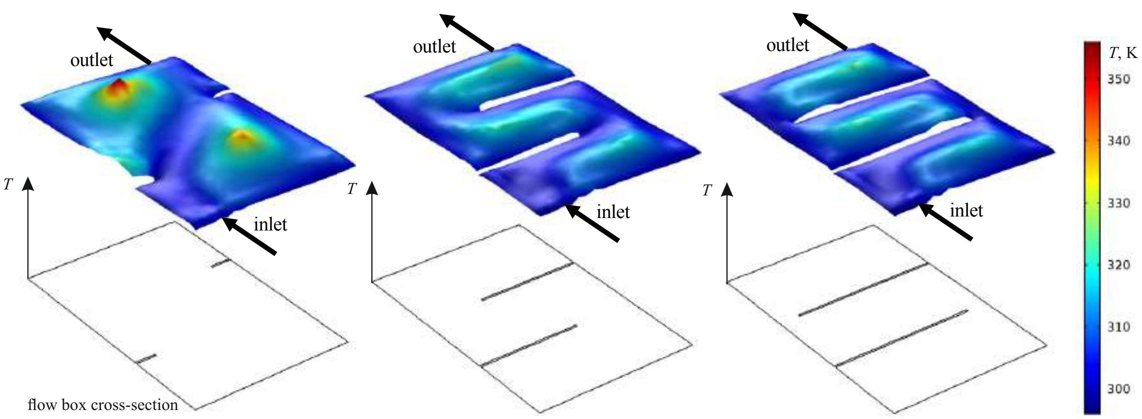

Figure 10: Single flow box of Fig. 1: temperature excess for water and the Base Case, with two 1 cm baffles (Left), two 5 cm baffles (Center), and two 7 cm baffles (Right). The temperature scale is provided at right. Inlet and outlet ports' positions are also provided.

baffles of 5 cm was the chosen option to reduce the overheating while decreasing the pressure drop with its associated increase of efficiency.

Conclusions

In this paper, a prototype of BCET technology was numerically studied and optimized. After validation, the original heater was modelled in 27 different conditions by varying the mass flow rate, the plate power and the fluid type to be heated.

The initial design of the prototype evidenced a pattern of heating inhomogeneity, for fluids that have viscosity and density similar to water. As strong excess temperature could be harmful to fluid features, a new design with different baffle lengths (from 1 to 7 cm) was examined. The optimal length of the baffles was found as 5 cm, which allowed to limit the uncontrolled temperature excess by almost 30%, decrease the difference between the maximum and minimum temperature by about 40%, while favouring the pressure drop reduction across the flow device by more than 10%.

Acknowledgements

This study received funding from the Spanish Ministerio de Economía y Competitividad, Technology Transfer Area, No DI-15-07519.

Author contributions statement

DA conceived the study and developed the analysis, in conjuction with GR. PC and GR developed the computational model and performed the computations, in conjunction with DA. GR wrote the manuscript. All Authors participated in manuscript revisions and discussion, coordinated and critiqued by GR.

Nomenclature

A	active surface area, m^2
B	baffle length, m
$c_{1\varepsilon}$	turbulence model parameter in Eq. (4)
$c_{2\varepsilon}$	turbulence model parameter in Eq. (4)
c_p	constant pressure specific heat, J/kgK
h	specific enthalpy, kJ/kg
k	turbulent kinetic energy, m^2/s^2
L	length, m
p	pressure, Pa
$\dot{q}$	heat flux, W/m^2
t	time, s
T	temperature, K
$\mathbf{v}$	velocity vector, m/s

v	velocity component, m/s
$\dot{V}$	volume flow rate, m^3/s
x, y, z	coordinates, m

Greek

Δt	process duration, s
ΔT	temperature increment, K
ε	turbulent energy dissipation rate, m^2/s^3
λ	thermal conductivity, W/mK
μ	dynamic viscosity, Pas
ρ	density, kg/m^3
σ_k	turbulence model parameter in Eq. (3)
σ_ε	turbulence model parameter in Eq. (4)
θ	dimensionless temperature
Ω	section area, m^2

Subscripts

i	inlet
max	maximum at the plate
min	minimum at the plate
o	outlet
p	single pass
t	turbulent

Superscripts

c	computational
m	control mass
v	control volume

References

[1] Owen, G. (2020). What makes climate change adaptation effective? A systematic review of the literature. Global Environmental Change, 62, 102071.

[2] Ladha-Sabur, A., Bakalis, S., Fryer, P. J., & Lopez-Quiroga, E. (2019). Mapping energy consumption in food manufacturing. Trends in Food Science & Technology, 86, 270-280.

[3] Makroo, H. A., Rastogi, N. K., & Srivastava, B. (2020). Ohmic heating assisted inactivation of enzymes and microorganisms in foods: A review. Trends in Food Science & Technology.

[4] Roberts, P. B. (2016). Food irradiation: Standards, regulations and world-wide trade. Radiation Physics and Chemistry, 129, 30-34.

[5] Ekezie, F. G. C., Sun, D. W., Han, Z., & Cheng, J. H. (2017). Microwave-assisted food processing technologies for enhancing product quality and process efficiency A review of recent developments. Trends in Food Science & Technology, 67, 58-69.

[6] Fernandez, J., Reyes-Davo, E., Reyes-Canovas, R., Garcia-Sevilla, J., Vela-Carrascosa, E., & Jara-Rico, A. (2015). Heating cell, heater using same, heating system and use thereof. ES2568749; PCT/ES, 70712, 2015.

[7] Fellows, P. J. (2009). Food processing technology: principles and practice, Chapter 8 p. 520. Elsevier.

[8] Deeth, H. C., & Lewis, M. J. (2017). High temperature processing of milk and milk products. John Wiley & Sons.

[9] Agcam, E., Akyildiz, A., & Dundar, B. (2018). Thermal pasteurization and microbial inactivation of fruit juices. In Fruit Juices (pp. 309-339). Academic Press.

[10] Zhang, Y., & Ma, H. B. (2008). Nonequilibrium heat conduction in a nanofluid layer with periodic heat flux. International journal of heat and mass transfer, 51(19-20), 4862-4874.

[11] Yang, J., Oh, S. R., & Liu, W. (2014). Optimization of shell-and-tube heat exchangers using a general design approach motivated by constructal theory. International Journal of heat and mass transfer, 77, 1144-1154.

[12] Picon-Nuñez, M., Polley, G. T., & Martinez-Rodriguez, G. (2013). Graphical tool for the preliminary design of compact heat exchangers. Applied thermal engineering, 61(1), 36-43.

[13] Caputo, A. C., Pelagagge, P. M., & Salini, P. (2008). Heat exchanger design based on economic optimisation. Applied thermal engineering, 28(10), 1151-1159.

[14] Ricci, R., Romagnoli, R., Montelpare, S., & Di Benedetto, D. (2014). Convective heat transfer increase in internal laminar flow using a vibrating surface. International journal of thermal sciences, 84, 358-368.

[15] Campet, R., Roy, P. T., Cuenot, B., Riber, E., & Jouhaud, J. C. (2020). Design optimization of an heat exchanger using Gaussian process. International Journal of Heat and Mass Transfer, 150, 119264.

[16] Kumar, S.D., Chandramohan, D., Purushothaman, K.,& Sathish, T., (2020). Optimal hydraulic and thermal constrain for plate heat exchanger using multi objective wale optimization. Materials Today Proceedings, 21, 876-881.

[17] Lofti, B., & Sundén, B. (2020). Thermo-hydraulic performance enhancement of finned elliptical tube heat exchangers by utilizing innovative dimple turbulators. Heat Transfer Engineering, 41, 1117-1142.

[18] Abeykoon, C. (2020). Compact heat exchangers design and optimization with CFD. International Journal of Heat and Mass Transfer, 146, 118766.

[19] Bicer, N., Engin, T., Yasar, H., Buyukkaya, E., & Aydin, A. (2020). Design optimization of a shell-and-tube heat exchanger with novel three-zonal baffle by using CFD and taguchi method. International Journal of Thermal Sciences, 155, 106417.

[20] Pepper, D. W., & Heinrich, J. C. (2017). The finite element method: basic concepts and applications with MATLAB, MAPLE, and COMSOL. CRC press.

[21] Ruocco, G. (2018). Introduction to Transport Phenomena Modeling: A Multiphysics, General Equation-Based Approach, pp. 106 and 166. Springer.

[22] COMSOL Multiphysics (2018) v. 5.2a. www.comsol.com. COMSOL AB, Stockholm, Sweden.

[23] Toledo, R. T., Singh, R. K., & Kong, F. (2007). Fundamentals of food process engineering, pp. 211. Springer.

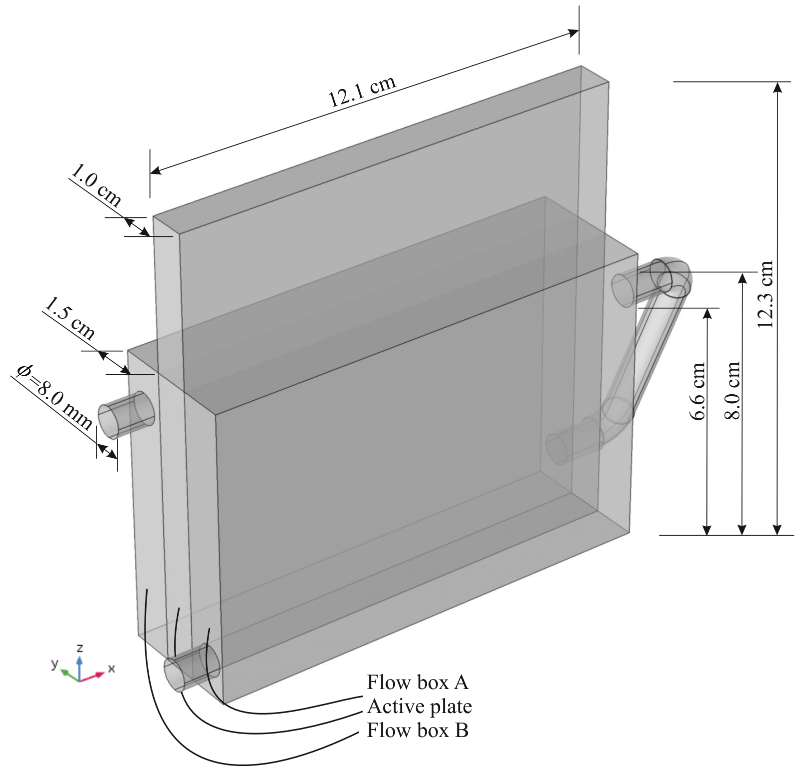

Figure 1: Configuration of the BCET prototype: two flow boxes A and B (including their pipe connections) interspersed by the active plate.

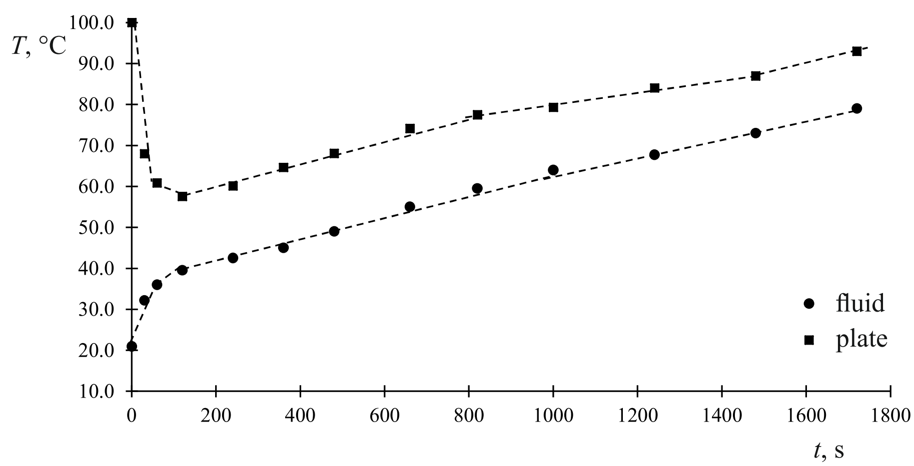

Figure 2: Typical progress of working fluid and plate temperatures.

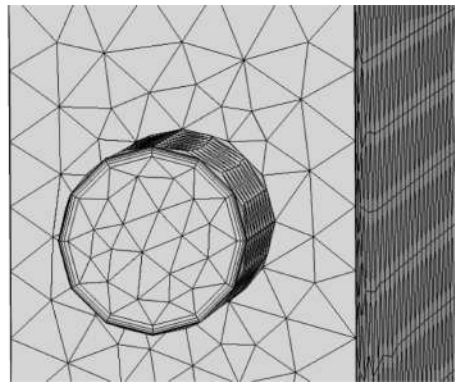

Figure 3: Close-up of the employed finite element grid of Fig. 4, featuring tetrahedral and boundary layer cells, before the flow box inlet. This kind of grid was adopted along all solid walls in the CV.

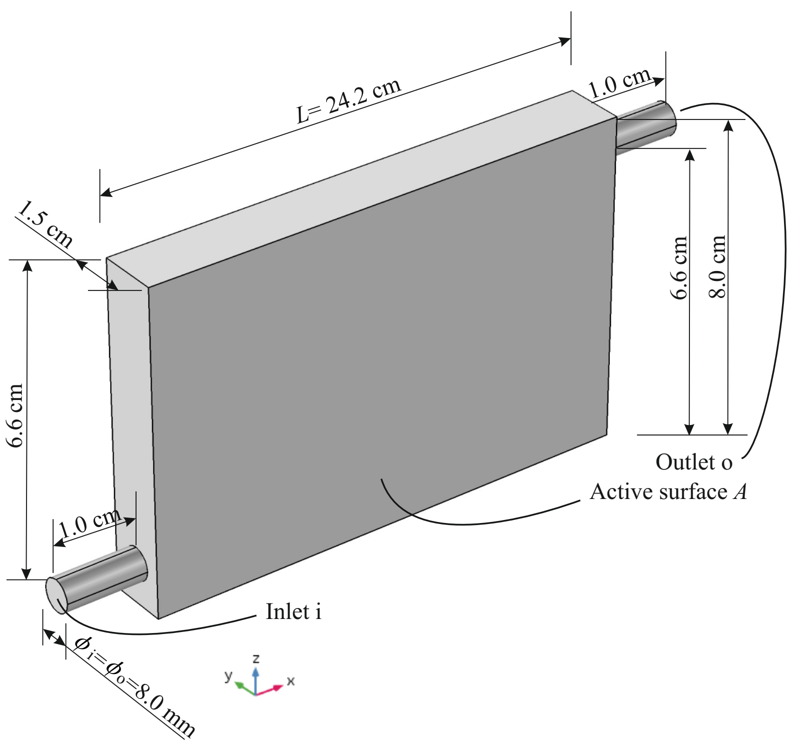

Figure 4: The modified flow box A. Here, an active surface A represents the active plate of Fig. 1.

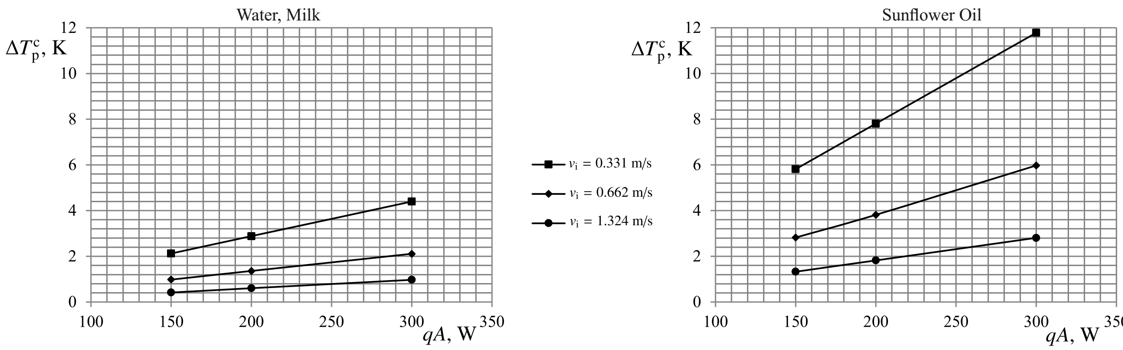

Figure 5: Single-pass temperature increases ΔT_p^c charts for the employed fluids, depending on the power applied to the active plate $\dot{q}A$ for variable inlet velocity v_i. Left: Water or Milk; Right: Sunflower Oil.

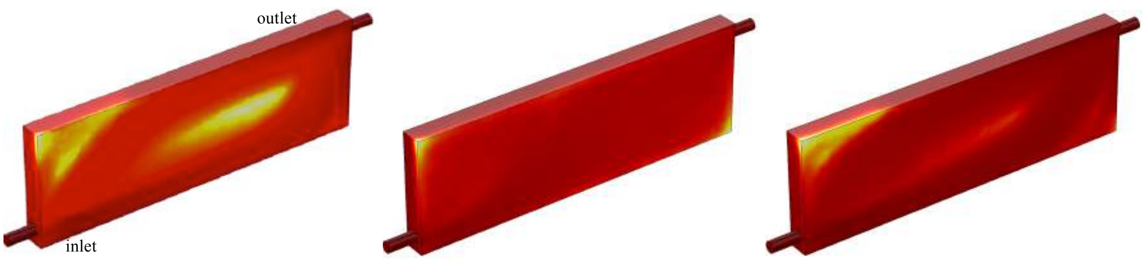

Figure 6: Flow box of Fig. 4: qualitative fluid temperature distributions adjacent to the active plate with L = 24.2 cm, when $\dot{q}A$ = 200 W and v_i = 0.662 m/s (Base Case). Left: Water; Center: Sunflower Oil; Right: Milk. The areas in yellow report on higher temperatures with respect to the various shades of red.

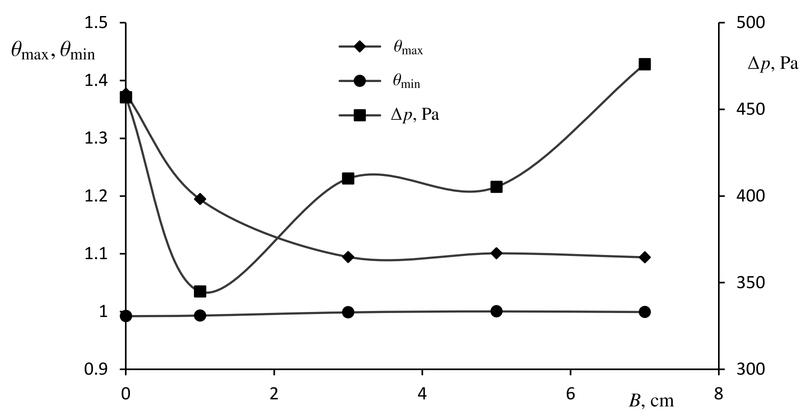

Figure 7: Single flow box of Fig. 1: dimensionless temperatures θ_{max} and θ_{min} at the active plate (left axis), and head loss Δp [Pa] (right axis), as dependent on baffle length B [cm], for the Base Case and milk.

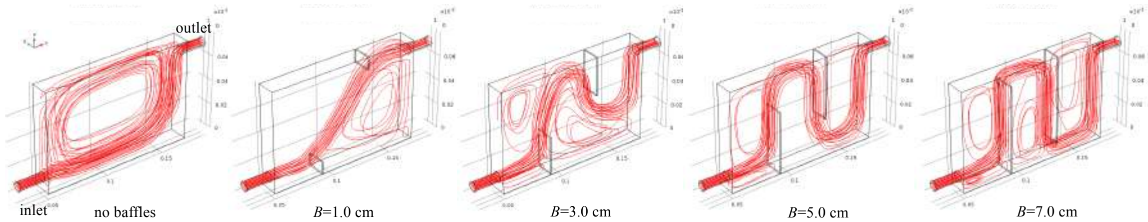

Figure 8: Single flow box of Fig. 1: the velocity field as streamline representation, for the five cases of Fig. 7, at increasing baffle length B. Dimensions are in [m].

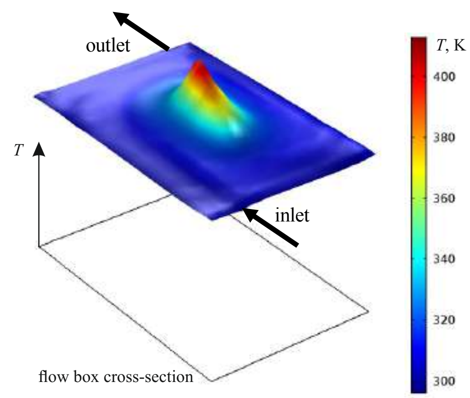

Figure 9: Single flow box of Fig. 1: temperature excess for water and the Base Case, with no baffles, with its scale at right. Inlet and outlet ports' positions are provided.

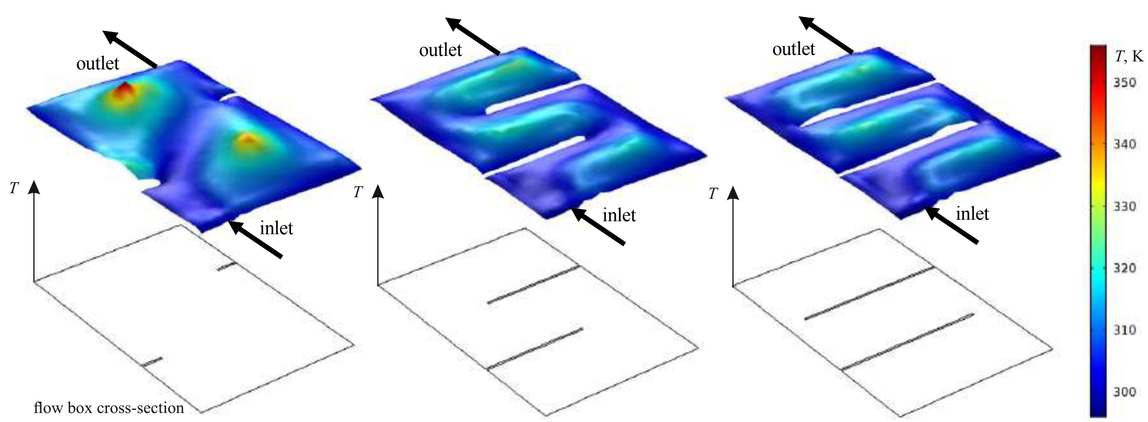

Figure 10: Single flow box of Fig. 1: temperature excess for water and the Base Case, with two 1 cm baffles (Left), two 5 cm baffles (Center), and two 7 cm baffles (Right). The temperature scale is provided at right. Inlet and outlet ports' positions are also provided.